*minerals*

MDPI

*Article*

# Depositional Setting of Archean BIFs from Congo: New Insight into Under-Investigated Occurrences

**Blandine Gourcerol [1,*], Olivier Blein [1], Matthieu Chevillard [1], Yannick Callec [1], Florent Boudzoumou [2] and Louis-Marie Joachim Djama [3,†]**

[1] French Geological Survey, BRGM, F-45060 Orléans, France; o.blein@brgm.fr (O.B.); m.chevillard@brgm.fr (M.C.); y.callec@brgm.fr (Y.C.)
[2] Geosciences Laboratory, Marien Ngouabi University, Brazzaville P.O. Box 69, Congo; florent.boudzoumou@umng.cg
[3] Directeur de la Géologie et des Mines, Brazzaville P.O. Box 69, Congo; lmdjama@hotmail.com
* Correspondence: b.gourcerol@brgm.fr
† Author passed away on 16 May 2020.

**Abstract:** Archean banded iron formations (BIF) represent a major contributor to better constraining and assessing the paleogeography and evolution of Archean cratons. In this context, we conducted an exhaustive sampling and analysis campaign of BIF units in the Congo Craton, covering several greenstone belts within the Ivindo, Kelle-Mbomo, and Chaillu blocks. The REE + Y patterns suggest: (1) Interaction of seawater with Fe-oxyhydroxides, as illustrated by strong REE enrichment coupled with La and Y enrichment; (2) contributions from high-temperature (>250 °C) hydrothermal fluids, illustrated by positive Eu anomalies; and (3) detrital input as suggested by relatively consistent REE concentrations and a chondritic Y/Ho ratio. These observations suggest a typical environment of Algoma-type BIF deposition. Moreover, assessment of the Ce anomalies in a combination of HREE enrichment indicates that some basins in the Chaillu and Ivindo blocks may have known potential oxygen-rich episodes in the early Archean during the deposition of these BIFs.

**Keywords:** BIF; Republic of the Congo; hydrothermal fluids; seawater; depositional settings; Chaillu; Ivindo; Kelle-Mbomo blocks; Congo Craton



**Citation:** Gourcerol, B.; Blein, O.; Chevillard, M.; Callec, Y.; Boudzoumou, F.; Djama, L.-M.J. Depositional Setting of Archean BIFs from Congo: New Insight into Under-Investigated Occurrences. *Minerals* **2022**, *12*, 114. https://doi.org/10.3390/min12020114

Academic Editor: Santanu Banerjee

Received: 10 December 2021
Accepted: 13 January 2022
Published: 19 January 2022



## 1. Introduction

Algoma-type banded-iron formations (BIF) are chemically formed sedimentary units consisting of alternating chert and iron-rich layers [1]. They are generally stratigraphically related to bimodal volcanic and sedimentary rocks in deformed and metamorphosed Archean to Early-Proterozoic greenstone belts [2,3]. These Fe-rich sedimentary units have long been considered a significant contributor for constraining and assessing the geochemical evolution of atmosphere and hydrosphere throughout the Precambrian [3–6]. Consequently, it is crucial to document and assess their geochemical characteristics.

Despite successive chemical transformations during diagenesis, or related to multiple metamorphic recrystallizations, the REE + Y abundance of BIFs reflects a geochemical signature indicative of their primary depositional environment [7–9]. This includes: (1) Interaction of seawater with Fe-oxyhydroxide and/or greenalite, as suggested by their strong REE enrichment coupled with positive La and Y anomalies; (2) contribution of high-temperature (>250 °C) hydrothermal fluids as suggested by positive Eu anomalies; and (3) detrital contributions, suggested by relatively flat REE patterns, high REE contents, and chondritic Y/Ho ratios (Y/Ho ≈ 25–27).

Here, we investigate the geochemical signatures of several BIFs from the Ivindo, Kelle-Mbomo and Chaillu Archean terrains within the Congo-Gabonian Craton in the Republic of the Congo (Figure 1). We also assess the depositional context of the BIFs within their host-rocks. In detail, the purpose of this paper is two-fold: (1) Document the BIF's

geochemical datasets; and (2) define the BIF's depositional settings at a regional scale, in a relatively poorly documented area when compared to the analogous, well documented BIFs from Cameroon [10–18] or Gabon [19].

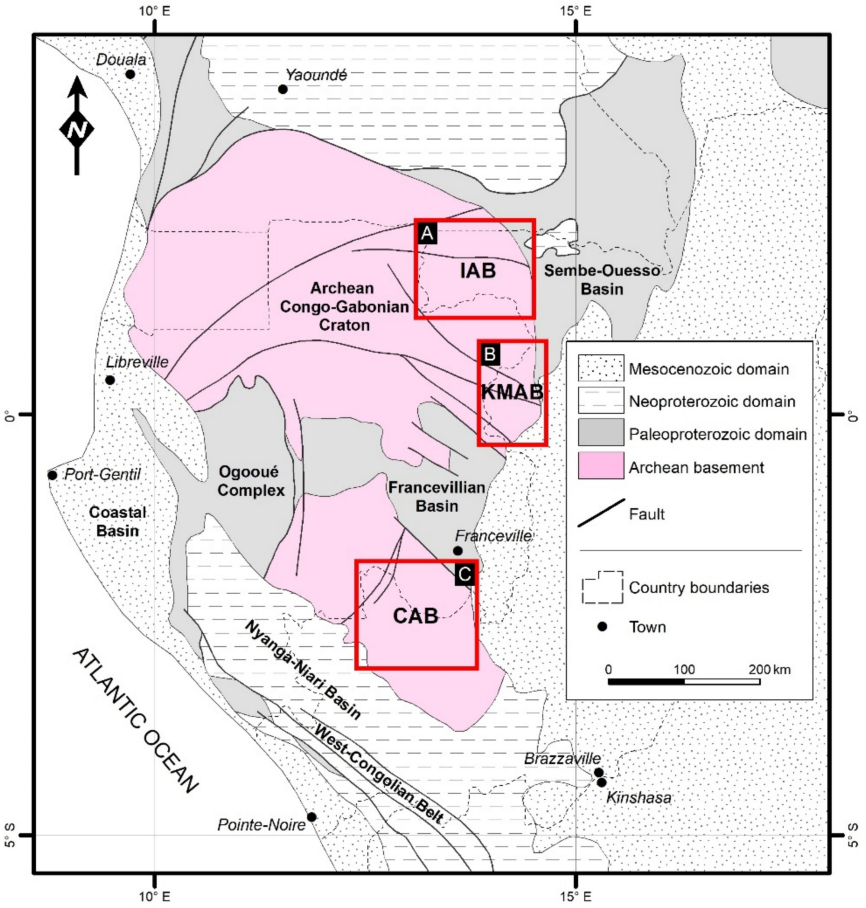


**Figure 1.** Simplified regional geological map of the Archean Congo-Gabonian Craton with location of studied areas (IAB: Ivindo Archean Block; KMAB: Kelle-Mbomo Archean Block; CAB: Chaillu Archean Block; modified from [20].

## 2. Regional Setting

The northwestern part of the Congo-Gabonian Craton in the Republic of the Congo comprises several exposed Archean nuclei, such as the Ivindo Block, the Kelle-Mbomo Block, and the Chaillu Block (Figures 1 and 2). In these blocks, the Archean rocks consist of three main suites and groups: (1) The 2.8 Ga Belinga Group of supracrustal rocks that are remnants of Mesoarchean greenstone belts [21,22]; (2) a Mesoarchean Gneissic Complex with tonalite-trondhjemite-granodiorite (TTG) affinities; and (3) a Mesoarchean to Neoarchean Granitoid Suite composed of magmatic bodies of sanukitoids and K-rich granitoids.

Geological mapping in the Ivindo, Kelle-Mbomo, and Chaillu Archean blocks, as part of the Congolese National Project of Geological Mapping, at 1/250,000 scale, acquired new field, geochemical, and geochronological data on the Archean rocks. U-Pb dates on zircons were determined in the BRGM laboratory, Orléans, France, using LA-ICP-MS with a quadrupole ICP-MS X series II coupled to a Cetac Excite 193 nm laser with ablation spot at 35 µm, energy pulses of 7J·cm–2, and repetition rates of 8 Hz [23–25].

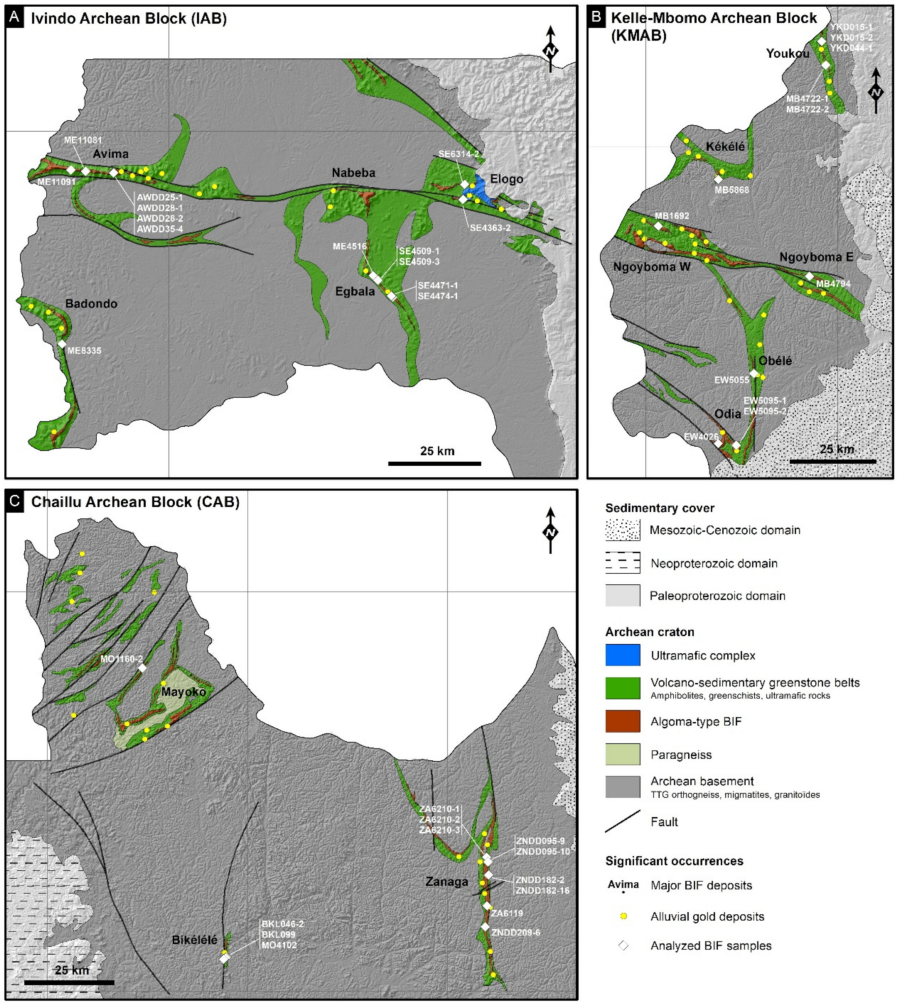


**Figure 2.** Architecture of the greenstone belts in the studied Congo Archean Blocks ((**A**): Ivindo; (**B**): Kelle-Mbomo, (**C**): Chaillu) and Algoma-type BIF distribution, with location of analysed samples (modified from [25–31]).

In the Republic of the Congo, the greenstone belts are older than 2850 Ma, as they were deformed and metamorphosed between 2800 and 2700 Ma (U-Pb dating on zircons) [23–25]. At the craton scale, these ages suggest an intense heat transfer from mantle to crust before 2.80 Ga and a major orogenic event around 2.75 Ga [23–25].

### *2.1. The Ivindo Archean Block*

The Ivindo Archean Block (IAB) lies in northern Gabon, northwest Congo, and southern Cameroon (Figure 2A). It consists of a granite-greenstone domain composed of a 3.0–2.7 Ga granitic Archean basement and ca. 2.8 Ga north- and west-trending greenstone belts forming the Belinga Group [20–22,26]. Several BIFs occur in this group and their age is estimated from 2866 to 2750 Ma [21]. In the Republic of the Congo, the greenstone belts surrounding BIFs have been essentially dated between 3080 and 2845 Ma (U/Pb dating on zircons) [23–25]. In southern Cameroon, however, whole-rock Pb-Pb dating yielded an age of 2679 Ma, interpreted as a metamorphic-reset age, suggesting that BIF deposition predates this age [16]. The basement includes granite, gneiss, and migmatite which underwent amphibolite to granulite facies metamorphism. Greenstone belts occur as disrupted belts in the Badondo, Avima, Nabeba, Egbala Monts, and Elogo areas. They are composed of ultrabasic rocks, amphibole-pyroxene rich rocks, amphibolite, metasedimentary rock, and BIFs, mostly metamorphosed from lower greenschist to amphibolite facies. Deformed

and/or migmatized TTG orthogneiss, with greenstone belt xenoliths and sanukitoid-like diorites and granodiorites, and syn- to post-tectonic biotite are common.

Mesocratic dioritic gneiss and felsic meta-volcanic rock within the Badondo greenstone belt yielded ages of 2914 Ma and 3080 Ma (U/Pb dating on zircon), respectively [25], and a meta-volcanic tuff within the Avima greenstone provided an age of 2878 Ma (all U/Pb dates on zircons) [25].

Description of the Sampled BIFs

From west to east, the Badondo and Avima Monts are approximately10-km-long oxide-facies BIF units consisting of alternating Fe-oxide-rich (magnetite and hematite rich) and chert bands affected by regional greenschist metamorphism [32–34]. They are mainly surrounded by schist and accessory unsubdivided amphibolite. Two main types of schist were identified in the field: (1) bright yellow mica schist suggesting a felsic metavolcanic affinity; and (2) greenish actinolite-chlorite schist. The latter amphibolite-schist sequence appears to have undergone low-grade greenschist regional retro-metamorphism [25].

In the Nabeba and Letioukabala Monts areas, oxide-facies BIFs at Egbala and Nabeba are surrounded by amphibolite and greenish actinolite-chlorite schist. Iron-carbonate bearing minerals such as siderite occur in the Nabeba BIF [34].

In the Elogo area, oxide-facies BIFs are surrounded by ultramafic rock, amphibolite, talc schist, and greenish actinolite-chlorite schist. Chert and Fe-rich layers, cm- to mm-scale, are dismembered and weakly oxidized.

### *2.2. The Kelle-Mbomo Archean Block*

The Kelle-Mbomo Archean Block (KMAB; Figure 2b), from which a schistose komatiitic basalt yielded an age of 2925 Ma for the Youkou greenstone belt [23], lies in the central part of Congo and Gabon. It is composed of deformed and/or migmatized TTG orthogneiss, northwest- to west-trending greenstone belts, mesocratic to melanocratic sanukitoid-like gneiss, and syn- to post-tectonic gray to pink biotite granite.

In the Kelle-Mbomo Block, greenstones occur as disrupted belts in the Youkou, Kékélé, Ngoyboma, Obélé, and Odia areas. These supracrustal rocks consist of BIF, amphibolite, ultramafic rocks, and paragneiss.

Description of the Sampled BIFs

From north to south in the Youkou area, BIF consists of cm- to dm-scale chert bands interbedded with minor magnetite to hematite layers. This unit is surrounded by talc and greenish actinolite-chlorite schist, with accessory amphibolite.

In the Obélé, Odia, and Kékélé areas, greenstones are characterized by oxide-facies BIF with amphibolite and accessory ultramafic rock and greenish actinolite-chlorite schist.

In the Ngoyboma area, BIF consists mainly of cm- to mm-scale, magnetite/hematite bands interbedded with minor mm-scale chert layers. They are associated with amphibolite, mesocratic gneiss and greenish actinolite-chlorite schist.

### *2.3. The Chaillu Archean Block*

The Chaillu Archean Block (CAB; Figure 2C) is continuous throughout the southern part of Gabon and Congo. It consists of ca. 3.1 to 2.54 Ga [35,36] deformed and/or migmatized TTG orthogneiss, northeast- and north-trending greenstone belts, mesocratic sanukitoid-like granodioritic gneiss, and syn- to post-tectonic, gray to pink, biotite granite.

Here, greenstone belts are disrupted in the Létoufou Mont (Bikélélé and Zanaga areas) and the Mayoko area. These supracrustal rocks consist mainly of oxide-facies BIF (magnetite and/or hematite), paragneiss, unsubdivided amphibolite, and ultramafic rock.

Two major plutonic events were identified in this block. They are expressed by: (1) Mesoarchean (2928 $\pm$ 6 Ma to 2870 $\pm$ 5 Ma–U/Pb dating on zircons) calc-alkaline granitoids [20], and (2) Neoarchean (2800–2550 Ma), alkaline to calc-alkaline magmatic

rock (syenite, granite, pegmatite), with both age ranges established by U/Pb dating on zircons [21].

Description of the Sampled BIFs

From west to east in the Mayoko area, a felsic meta-volcanic rock and an amphibolite were dated at 2883 Ma and 2864 Ma (U/Pb dating on zircons), respectively [22]. Oxide-facies BIFs generally comprise well developed, cm- to mm-thick chert and magnetite/hematite bands. They are surrounded by amphibolite, talc schist, and greenish actinolite-chlorite schist. Ultramafic rocks are rare.

The Bikélélé BIFs consist of cm- to mm-thick silicate-rich chert bands interbedded with oxide-rich bands. They are interstratified with amphibolite, ultramafic rock, and greenish actinolite-chlorite schist and are surrounded by mesocratic gneiss.

The Zanaga BIF consists of mm-thick chert and magnetite/hematite layers with local amphibolitic material. Locally disrupted chert bands are described as "dirty" layers, suggesting the presence of detrital material. Amphiboles occur at the boundaries of the Fe-rich and Si-rich bands (Figure 2A).

## 3. Materials and Methods

Exposed BIFs were sampled during regional geological mapping by the BRGM from 2013 to 2015 (Figure 2). Descriptions of these BIFs are given in their regional-setting sections. They vary from silicate- to oxide-facies BIFs, with variable amounts of chert. The samples for this study include: (1) 14 samples from the Ivindo Block (Avima, Badondo, Egbala and Elogo); (2) 12 samples from the Kelle-Mbomo Block (Kékélé, Ngoyboma, Obélé and Odia); and (3) 13 samples from the Chaillu Block (Mayoko, Zanaga and Bikélélé) (Figure 2). Figure 3 shows photographs of these BIF samples.

*Whole-Rock Analyses*

As this study is a first approach for these new BIF occurrences, we followed suggestions in recent work, to adopt whole-rock analyses for representing the prevailing local to regional paleoenvironmental conditions [6]. It is known that both magnetite and hematite as well as Si-rich layers from BIFs retain the primary REE + Y geochemical signature [7,9,37], though detrital components, which cannot be precisely identified in LA ICP MS analyses, can also influence the REE + Y pattern [7]. However, we consider that this detrital component is part of the primary signature, thus constraining part of the regional paleogeography.

The analyses were performed by the ALS Minerals laboratory. $SiO_2$, $Al_2O_3$, $Fe_2O_3{}^T$, CaO, MgO, $Na_2O$, $K_2O$, $Cr_2O_3$, $TiO_2$, MnO, $P_2O_5$, SrO, BaO, and LOI were determined by aqua regia digestion and inductively coupled plasma-atomic emission spectrometry (ICP-AES) analysis with the ALS Minerals ME-ICP06 method. Ag, As, Cd, Co, Cu, Li, Mo, Ni, Pb, Sc, Tl, and Zn were determined by four-acid ($HNO_3$, $HCLO_4$, HF, and HCL) digestion and ICP-AES analysis with the ALS ME-4ACD81 method.

Trace and rare earth elements, such as Ba, Ce, Cr, Cs, Dy, Er, Eu, Ga, Gd, Ce, Hf, Ho, La, Lu, Nb, Nd, Pr, Rb, Sm, Sn, Sr, Ta, Tb, Th, Tm, U, V, W, Y, Yb, and Zr were determined by lithium borate fusion prior to acid ($HNO_3$ and HCl) dissolution and followed by inductively coupled plasma–mass spectroscopy (ICP-MS) analysis (ALS-ME-MS81 method). As, Bi, Hg, In, Re, Sb, Se, Te, and Tl were determined by aqua regia digestion followed by ICP-MS analysis (ALS-ME-MS42 method). Finally, C and S were analyzed by LECO furnace (C-IR07 and S-IR08 methods respectively).

Various ALS standards were used and data quality was assured by running standards CCU-1d, EMOG-17, GRE-3, GS310-7, GS311-3, and GS910-4 between samples as unknowns. The detection limits varied from 0.01 to 0.03 ppm for REE + Y.

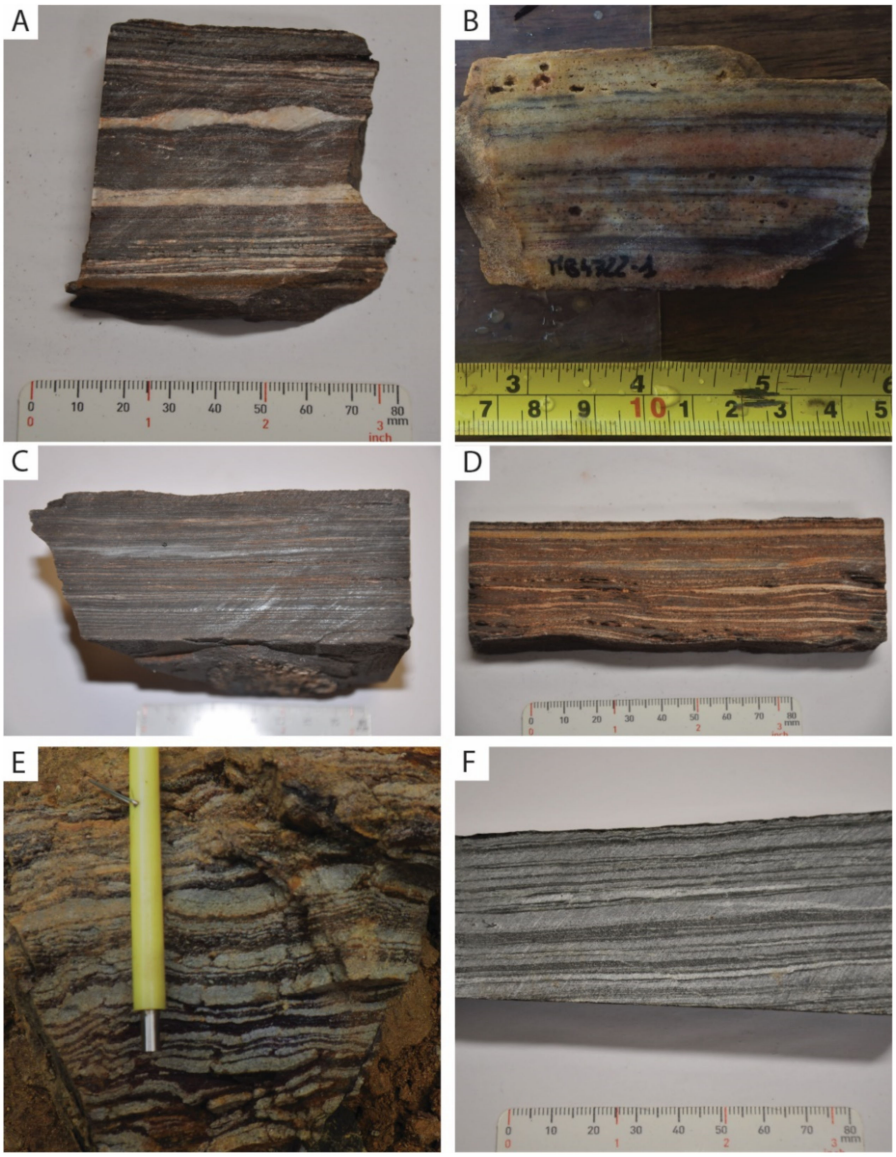


**Figure 3.** Photographs of outcrop BIF samples from selected units. (**A**) Avima BIF sample (ME11081); (**B**) Youkou BIF sample (MB4722-1); (**C**) Elogo BIF sample (SE4363-2); (**D**) Egbala BIF sample (SE4474-1); (**E**) Bikélélé BIF sample (MO4102-2); and (**F**) Zanaga BIF sample (ZNDD209-6).

The Queensland alluvial shale composite (MUQ) [38], which reflects a bimodal, mafic, and felsic component typical of Archean greenstone belts, was used for normalizing the REE + Y concentrations, in order to minimize the influence of potential terrigenous input.

La, Ce, Eu, and Y anomalies were calculated following the equations of [38]:

$$La/La^{*}MUQ = LaMUQ/(PrMUQ * (PrMUQ/NdMUQ)\ 2) \quad (1)$$

$$Ce/Ce^{*}MUQ = CeMUQ/(PrMUQ * (PrMUQ/NdMUQ)) \quad (2)$$

$$Eu/Eu^{*}MUQ = EuMUQ/(SmMUQ2 * TbMUQ)\ 1/3 \quad (3)$$

$$Y/Y^{*}MUQ = YMUQ/(0.5Er\ MUQ * 0.5Ho\ MUQ) \quad (4)$$

La and Ce anomalies were calculated separately, as both can be representative of true anomalies.

## 4. Results

### *4.1. REE + Y Systematics*

Despite a few exceptions, the REE + Y normalized data show relatively uniform REE + Y patterns (Figures 4–6; Table S1).

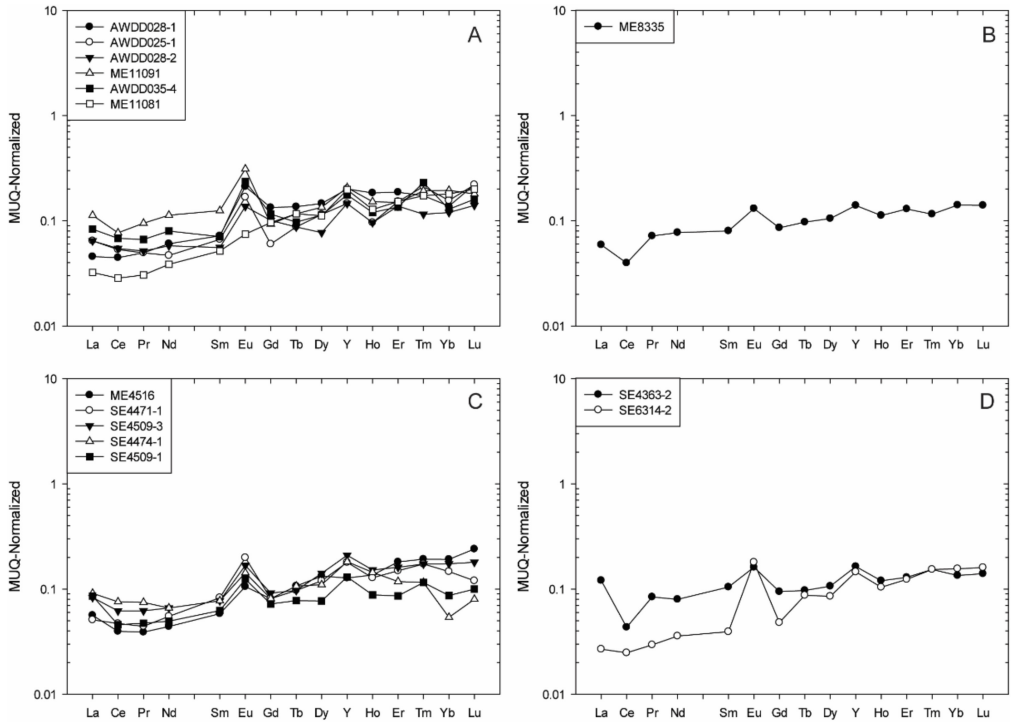


**Figure 4.** MUQ-normalized REE + Y patterns for BIF samples from different parts of the Ivindo Block: (**A**) Avima, (**B**) Badondo, (**C**) Egbala, and (**D**) Elogo.

#### 4.1.1. The Ivindo Archean Block

The Avima (Figure 4A), Badondo (Figure 4B), Egbala (Figure 4C), and Elogo (Figure 4D) BIF units are characterized by relatively consistent REE + Y patterns:

- All samples from the Avima BIF unit show HREE enrichment (Nd/YbMUQ = 0.21–0.62), well developed positive La, Y, and Eu anomalies (La/La*MUQ = 1.16–1.81, Y/Y*MUQ = 1.08–1.40, Eu/Eu*MUQ = 1.07–2.93), and super-chondritic to chondritic Y/Ho values (Y/Ho = 28.69–38.66). Weakly-positive to positive Ce anomalies are reported for these samples (Ce/Ce*MUQ = 0.96–1.23) (Figure 4A).
- The ME8335 sample from the Badondo BIF unit shows enrichment in HREE relative to LREE (Nd/YbMUQ = 0.54), has positive Y and Eu anomalies (Y/Y*MUQ = 1.15, Eu/Eu*MUQ = 1.49) related to a non-depletion of La (La/La*MUQ = 0.95), and a super-chondritic Y/Ho ratio (Y/Ho = 32.85). A strongly developed negative Ce anomaly is reported for this sample (Ce/Ce*MUQ = 0.59) (Figure 4B).
- Most Egbala BIF unit samples show HREE enrichment (Nd/YbMUQ = 0.21–0.62), except SE4474-1 that shows only enrichment of LREE relative to MREE (Nd/YbMUQ = 1.22, Pr/SmMUQ = 0.96). Slightly negative to strongly positive to La, Y, and Eu anomalies and chondritic to super-chondritic Y/Ho values are reported for this BIF unit (La/La*MUQ = 0.95–1.84, Y/Y*MUQ = 0.80–1.49, Eu/Eu*MUQ = 1.44–2.22, Y/Ho = 24.70–39.09). Slightly negative to moderately positive Ce anomalies are shown for these samples (Ce/Ce*MUQ = 0.89–1.32) (Figure 4C).
- All samples from the Elogo BIF unit show HREE enrichment (Nd/YbMUQ = 0.21–0.62), well developed positive La, Y, and Eu anomalies (La/La*MUQ = 1.03–1.34, Y/Y*MUQ = 1.05–1.31, Eu/Eu*MUQ = 1.45–3.40), and super-chondritic Y/Ho values

(Y/Ho = 30.35–36.92). Variable Ce anomalies are reported for these samples (Ce/Ce*MUQ = 0.48–1.02) (Figure 4D).

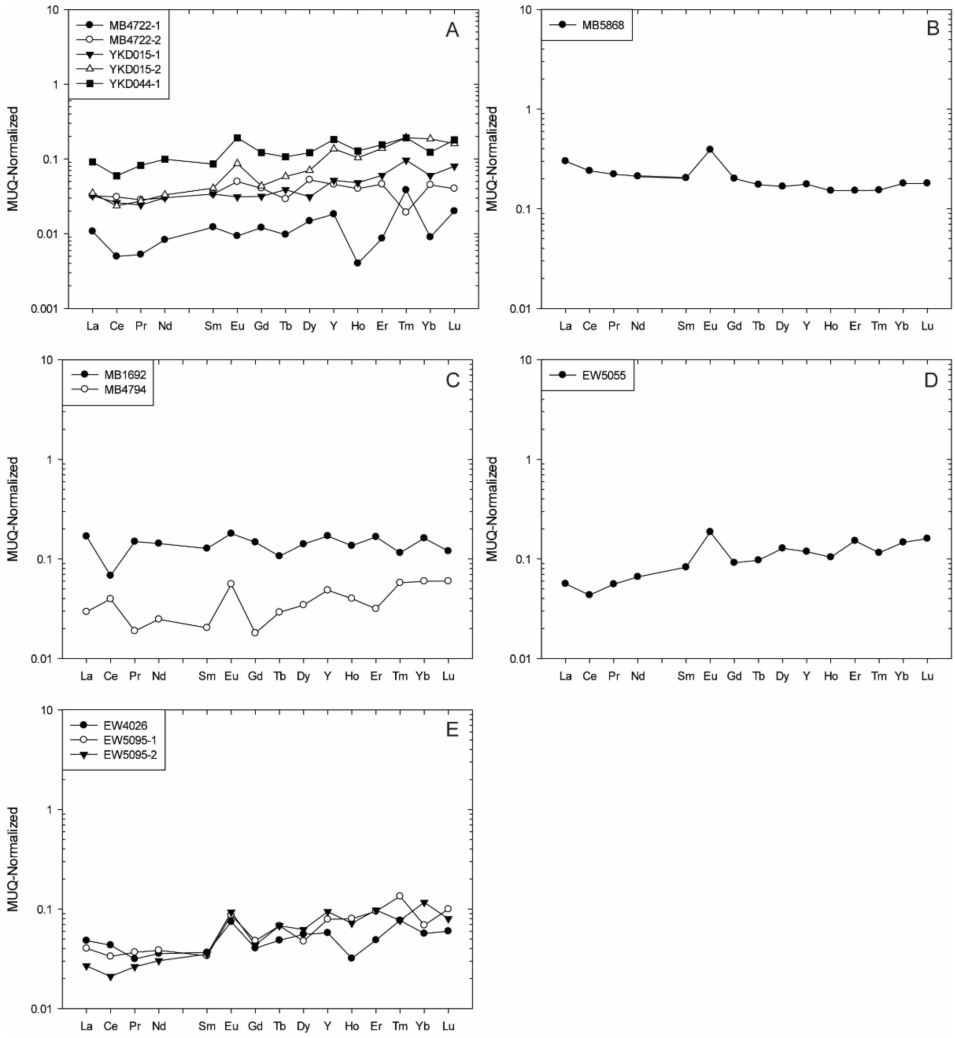


**Figure 5.** MUQ-normalized REE + Y patterns for BIF samples in different parts of the Kelle-Mbomo Block: (**A**) Youkou, (**B**) Kékélé, (**C**) Ngoyboma, (**D**) Obélé, and (**E**) Odia.

#### 4.1.2. The Kelle-Mbomo Archean Block

The Youkou (Figure 5A), Kékélé (Figure 5B), Ngoyboma (Figure 5C), Obélé (Figure 5D), and Odia (Figure 5E) BIF units are characterized by relatively consistent REE + Y patterns:

- All samples from the Youkou BIF unit show relative HREE enrichment to relatively flat patterns (Nd/YbMUQ = 0.17–0.91), faintly negative to strongly positive La and Y (La/La*MUQ = 1.28–5.01, Y/Y*MUQ = 0.95–2.88), and variable Eu and Ce anomalies (Eu/Eu*MUQ = 0.78–2.04, Ce/Ce*MUQ = 0.87–1.47) along with chondritic to super-chondritic Y/Ho values (Y/Ho = 28.33–120) (Figure 5A).
- Sample MB5868 from the Kékélé BIF unit shows a relatively flat REE pattern (Nd/YbMUQ = 1.17). It also has a positive La anomaly (La/La*MUQ = 1.23) related to the non-depletion of Y (Y/Y*MUQ = 1.15), a positive Eu anomaly (Eu/Eu*MUQ = 1.98), and a super-chondritic Y/Ho ratio (Y/Ho = 30.52). A positive Ce anomaly is reported for this sample as well (Ce/Ce*MUQ = 1.03) (Figure 5B).
- The two samples from the Ngoyboma BIF unit have similar features, showing depletion in HREE enrichment (Nd/YbMUQ = 0.41–0.88), positive La, Y, and Eu (La/La*MUQ = 1.03–2.66, Y/Y*MUQ = 1.12–1.35, Eu/Eu*MUQ = 1.46–2.34), and

variable Ce anomalies (Ce/Ce*MUQ = 0.43–2.73), along with super-chondritic Y/Ho values (Y/Ho = 32–32.94) (Figure 5C).

- Sample EW5055 from the Obélé BIF unit shows enrichment in LREE relative to HREE (Nd/YbMUQ = 0.45), slightly negative to moderately positive La, Y, and Eu (La/La*MUQ = 1.41, Y/Y*MUQ = 0.92, Eu/Eu*MUQ = 2.08), and a super-chondritic Y/Ho ratio (Y/Ho = 30). A non-depletion Ce anomaly is reported for this sample (Ce/Ce*MUQ = 0.91) (Figure 5D).
- All samples from the Odia BIF unit show enrichment in LREE relative to HREE (Nd/YbMUQ = 0.25–0.62), slightly negative to moderately positive La, Y, and Eu (La/La*MUQ = 1.02–1.96, Y/Y*MUQ = 0.90–1.55, Eu/Eu*MUQ = 1.41–2.05), and chondritic to super-chondritic Y/Ho values (Y/Ho = 26–50). Variable Ce anomalies are reported for these samples a well (Ce/Ce*MUQ = 0.70–1.55) (Figure 5E).

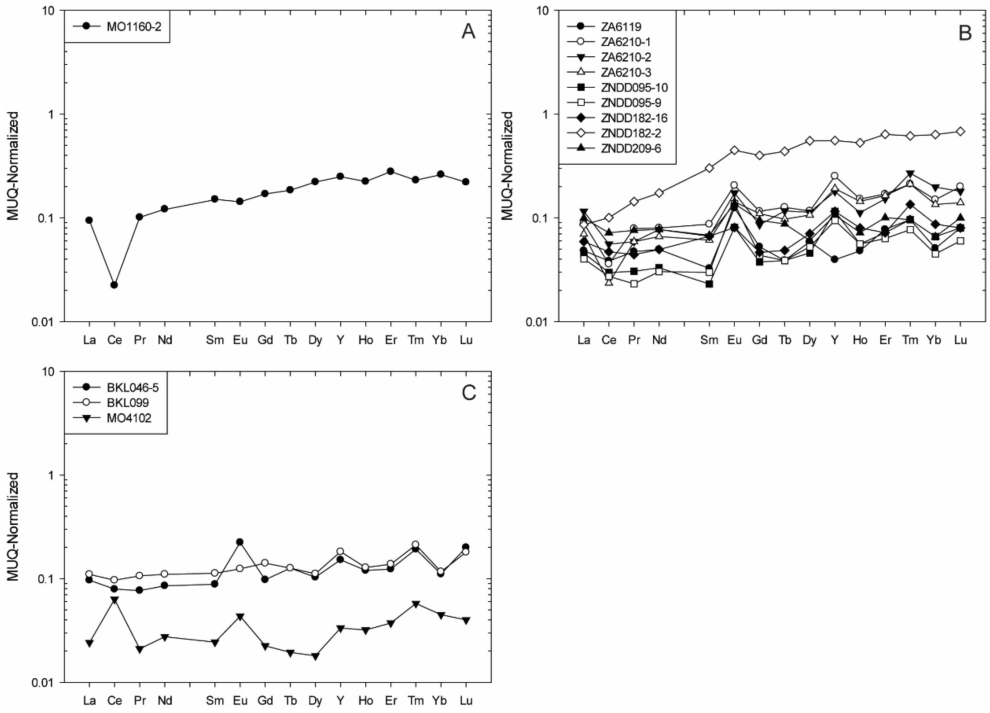


**Figure 6.** MUQ-normalized REE + Y patterns for BIF samples in different parts of the Chaillu Block: (**A**) Mayoko, (**B**) Zanaga, and (**C**) Bikélélé.

#### 4.1.3. The Chaillu Archean Block

The Mayoko (Figure 6A), Zanaga (Figure 6B), and Bikélélé (Figure 6C) BIF units yielded relatively consistent REE + Y patterns:

- Sample MO1160-2 from the Mayoko BIF unit is enriched in HREE relative to LREE (Nd/YbMUQ = 0.46), has a positive La anomaly (La/La*MUQ = 1.33) related to non-depletion of Y (Y/Y*MUQ = 0.99), a weak negative Eu anomaly (Eu/Eu*MUQ = 0.87), and a super-chondritic Y/Ho ratio (Y/Ho = 29.28). The sample also has a strongly developed negative Ce anomaly (Ce/Ce*MUQ = 0.26).
- The three samples from Bikélélé show LREE depletion (Nd/YbMUQ = 0.61–0.94), positive La, Y, and Eu anomalies (La/La*MUQ = 1.03–2.19, Y/Y*MUQ = 0.96–1.37, Eu/Eu*MUQ = 1.03–2.19), and chondritic to weakly super-chondritic Y/Ho values (Y/Ho = 27.5–33.3). Weakly-positive to positive Ce anomalies are reported for these samples (Ce/Ce*MUQ = 0.94–3.92).
- Most samples from the Zanaga BIF unit have relatively uniform REE + Y patterns with HREE enrichment, positive La, Y, and Eu anomalies, and chondritic to super-chondritic

Y/Ho values (Nd/YbMUQ = 0.27–0.97, La/La*MUQ = 1.11–3.34, Y/Y*MUQ = 1.23–1.80, Eu/Eu*MUQ = 1.29–4.05, Y/Ho = 27.7–54.28). However, a few variations occur:

1. The ZNDD209-6 sample varies by its weak depletion in HREE relative to LREE (Nd/YbMUQ = 1.17), and ZA6119 by its negative Y anomaly (Y/Y*MUQ = 0.62)
2. The ZNDD182-2 sample varies by its weakly developed negative La and Y anomalies (La/La*MUQ = 0.87, Y/Y*MUQ = 0.95).
3. For Ce anomalies, two distinct sample groups are identified: (1) with weak to moderate positive Ce anomalies (Ce/Ce*MUQ = 0.96–3.92); and (2) four samples (i.e., ZA6119, ZA6210-1, ZA6210-3, ZNDD182-2) with strongly to moderately developed negative Ce anomalies (Ce/Ce*MUQ = 0.84–0.44).

### *4.2. Additional Major- and Trace-Element Data*

BIF samples from the selected areas show similar overall abundances of major and trace elements (Figure 7) with few variations. As expected, $SiO_2$ (28.14 to 98.33 wt.%) and $Fe_2O_3t$ (1.52 to 64.03 wt.%) show relatively high concentrations related to intrinsic geochemical compositions of the BIFs.

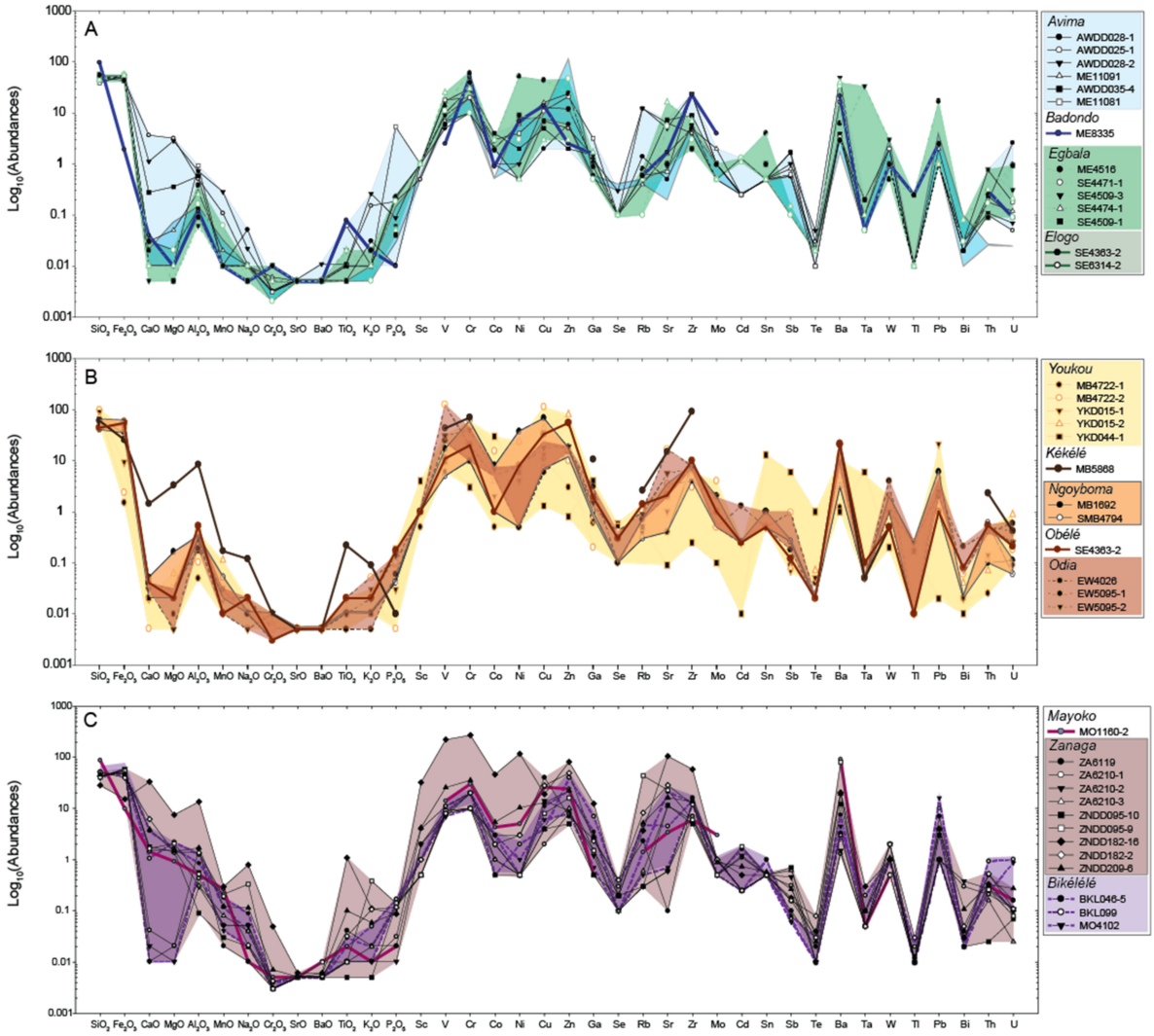


**Figure 7.** Spider-type diagrams summarizing the abundance of major and trace elements for BIF from the Ivindo (**A**), Kelle-Mbomo (**B**) and Chaillu (**C**) blocks.

For most of the samples, $Al_2O_3$ and $TiO_2$ are both <0.9 wt.%. Both oxides may reflect clay and/or detrital input. Samples from silicate-BIFs, such as those from the Bikélélé (BLK099, MO4128), Zanaga (ZA6119, ZNDD182-2 and ZNDD209-6), and Kékélé (MB5868) BIF units, show higher $Al_2O_3$ (1.26–12.66 wt.%), TiO2 (>0.04 wt.%), and $Na_2O$ (>0.05 wt.%) contents.

In the IAB, the AWDD020-1 and AWDD028-2 samples show high Ba contents (16.3 and 49.8 ppm, respectively) and AWDD028-2 has a high Zr content (24 ppm) both compared to the same locality (Figure 7a). The Badondo sample (ME8335) shows relatively high Ba (21.7 ppm), Cr (50 ppm), Zr (23 ppm), Ni (7 ppm), and Cu (14 ppm) concentrations. In the Egbala area, ME4516 has high Cr (60 ppm), Ni (52 ppm), Cu (44 ppm), and Pb (17 ppm) concentrations. SE4471-1 shows high Ba (34.2 ppm), Sr (5.5 ppm), and Zn (47 ppm) contents compared to the same locality.

In the KMAB, the Youkou BIF samples have a high $SiO_2$ content (98.33–51.09 wt.%). The MB4722-2 sample shows high Ba (11.8 ppm), Cr (60 ppm), Sr (3.5 ppm), Cu (113 ppm), Co (15.4 ppm), and Ni (23 ppm) contents. The MB5868 sample has high Ba (20.4 ppm), Cr (70 ppm), Ga (10.6 ppm), Sr (14.8 ppm), Th (2.3 ppm), V (43 ppm), and Zr (91 ppm) concentrations (Figure 7b).

The EW5055 Obélé BIF sample shows high Zn (55 ppm) and the EW5095 sample from the Odia BIF unit has a high V (126 ppm) content.

In the CAB, concentrations of immobile crustal trace elements (Zr, Th, Sc, and Hf) are variable in selected BIFs (Figure 7c). In the Zanaga area (CAB), the ZNDD182-2 sample has relatively high MgO (2.05 wt.%), K2O (0.38 wt.%), Ba (80 ppm), Ga (12.4 ppm), Sr (105 ppm), Cr (270 ppm), Rb (3.7 ppm), V (222 ppm), Zr (58 ppm), Co (46 ppm), Ni (117 ppm), and Zn (81 ppm) contents compared to the other samples from the same locality. The ZNDD209-6 sample shows high contents for a few of these elements (Ba = 20 ppm; Rb = 8.2 ppm; Sr = 28.4 ppm; Cr = 20 ppm; Zr = 12 ppm; Cu = 28 ppm; Zr = 49 ppm). The Mayoko sample has relatively high Ba (90.9 ppm), V (14 ppm), Co (4.3 ppm), Pb (10 ppm), and Zr (6 ppm) contents compared to the other samples.

## 5. Discussion

### *5.1. Primary Signatures*

Several parameters (primary versus secondary inputs) can influence the REE + Y patterns. First of all, it has been demonstrated that the detrital component can strongly influence the primary signature by flattening the REE + Y spectra and mitigating seawater anomalies [6]. However, this input is part of the syn-depositional sedimentary component of the BIF, contributing to its REE + Y budget, and thus has to be studied. Moreover, normalization to MUQ (terrigenous composite for Archean greenstone belt) aims at minimizing the influence of potential detrital input on the REE + Y signal.

Secondly, secondary weathering can affect major- and trace-element budgets. Regarding the REE + Y content, Ce is considered as one of the most robust redox proxies due to the general insolubility of REE at Earth surface conditions, by its immobility during metamorphism [7], and by the fact that Ce becomes more immobile when oxidized [39]. Some studies on BIFs suggest that negative excursions of Ce/Ce* may reflect atmospheric oxygenation [40]. Recent work has highlighted that a negative Ce anomaly, when combined with extreme LREE enrichment relative to HREE, reflects secondary weathering in BIFs sampled from the Barberton Greenstone Belt in South Africa [39]. Thus, Ce must be studied carefully for potential post-depositional alteration in complement to LREE enrichment, in order to reveal such processes and modifications of the REE spectra.

However, in our case, the consistency of REE patterns suggests that the primary signal is relatively well preserved in most BIF units. Many samples show depletion in LREE relative to HREE, as well as positive La, Y, and Eu anomalies, suggesting BIF deposition of the BIF units in seawater under the influence of high-temperature (>250 °C) hydrothermal fluids [7,41,42]. This type of environment is typical of Algoma-type BIFs [43,44].

Despite these observations, samples from the Ngoyboma BIF unit and a few from the Youkou BIF unit, both of which petrographically show strong hematization, have an erratic or flatter REE-Y pattern that suggests potential REE-remobilization, related to either late alteration, or lateritic weathering. In addition, it appears that HREE are remobilized more easily than LREE (cf. erratic pattern), which was observed elsewhere [45,46].

#### 5.1.1. Assessment of High-Temperature (>250 °C) Hydrothermal Fluids

Most samples show the influence of seawater and high-temperature hydrothermal fluids through their REE + Y patterns and La, Y, and Eu anomalies [41,42], as mentioned above. Assessment of a high-temperature hydrothermal-fluid component during BIF precipitation uses Sm/Yb versus Eu/Sm ratios [7,47]. A binary mixing line was calculated between North Pacific seawater samples [48] and an Archean chert breccia sample from the 2.7 Ga Abitibi greenstone belt [44] shows an extremely strong Eu anomaly [7]. This suggests that the sample location was exceptionally close to the hydrothermal source (Figure 8).

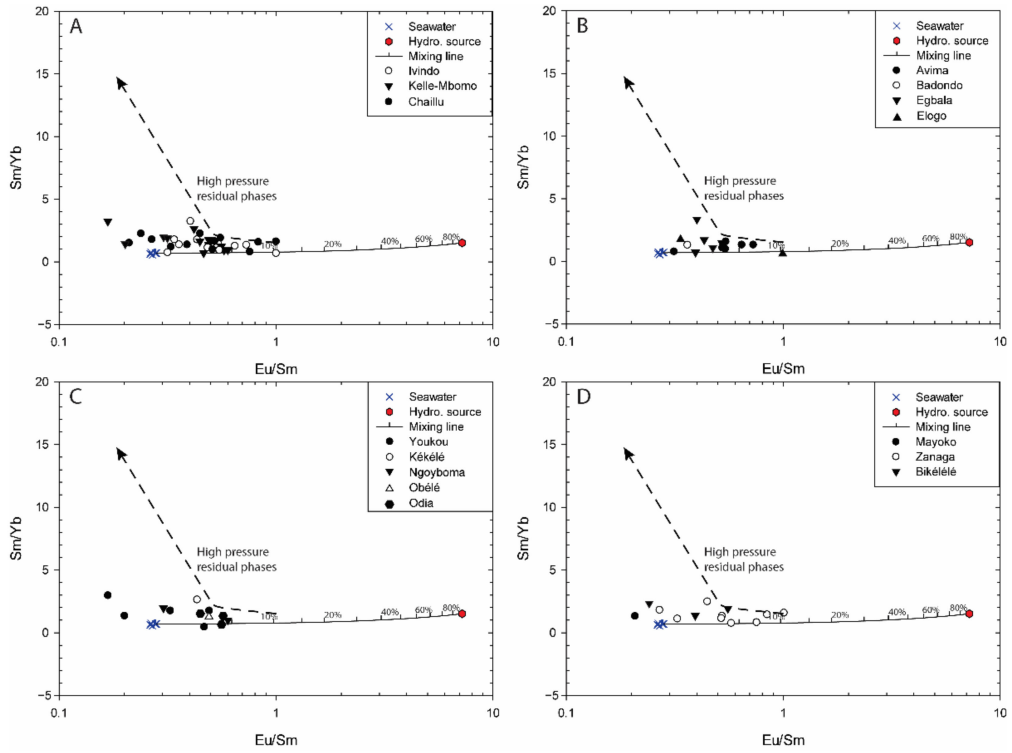


**Figure 8.** Binary plots of elemental ratio data (Eu/Sm and Sm/Yb) for BIF samples from the Ivindo (**A**,**B**), Kelle-Mbomo (**A**,**C**) and Chaillu (**A**,**D**) blocks. These plots are used for assessing the potential influence of high-T hydrothermal fluids on BIF chemistry, as illustrated by the conservative mixing line. High-T hydrothermal fluid data are from [44]) and seawater data are from [48].

Most samples are distributed along, or a little above, a mixing line like the Sm/Yb one in Figure 8. This may reflect the presence of high-pressure residual phases, such as garnets, amphiboles, etc., which are relatively common in metamorphic sedimentary rocks from greenstone belts. However, all samples indicate a consistent hydrothermal influence of up to 10%. This is similar to Algoma-type BIFs in Canada or Brazil [7,9] and can be used as a proxy for the locus of BIF-precipitation relative to a hydrothermal-source vent. It also indicates a relative distance for an Algoma-type BIF depositional site.

Interestingly, the distribution of BIFs within each Archean block may indicate their geographical location relative to the hydrothermal plumes from which BIFs are deposited [7]. Thus, in the IAB, the Badondo BIF unit appears to be less affected by hydrothermal-vent processes (farther away) than the Egbala and the Avima BIFs (Figure 8B).

In the KMAB, the Youkou BIF unit is less affected by hydrothermal fluids than the Kékélé/Obélé and Odia BIF units, suggesting that the Odia unit was located closer to the hydrothermal source (Figure 8C).

Similarly, in the CAB, the Mayoko BIF unit appears less affected by hydrothermal processes than, first, the Bikélélé and then the Zanaga BIFs. This suggests that the Mayoko BIF unit was probably deposited farther way from a hydrothermal source than the Bikélélé and the Zanaga BIFs (Figure 8D).

However, estimating a distance to hydrothermal sources for the other BIFs would be a bit adventurous, requiring much more data.

#### 5.1.2. Assessment of Redox Conditions

In modern oxic seawater, a relatively well-developed negative Ce anomaly is generally due to the scavenging of Ce by Fe-Mn oxyhydroxides, leading to the oxidation of $Ce^{3+}$ to $Ce^{4+}$ [48]. In sub-oxic to anoxic seawater, such REE removal does not occur because of the reductive dissolution of settling Mn-(Fe) rich particles [3,49–51]. However, in an oxygenated closed basin, Bau [51] demonstrated that pH conditions strongly affect Ce anomalies, producing a positive Ce excursion when pH $\leq$5 and a negative Ce anomaly when pH $\geq$5.

In the context of Algoma-type BIF precipitation, Fe-oxyhydroxide precipitation causes scavenging of La, Y, (Gd), and LREE, providing a pure seawater geochemical signature. However, in a restricted basin without continuous recharge of the REE-Y budget induced by seawater excursions, negative La and Y anomalies can be observed (Figure 9). Thus, basin dynamics can be assessed using Ce, La, and Y anomalies and Y/Ho values below the chondritic value of about 25.

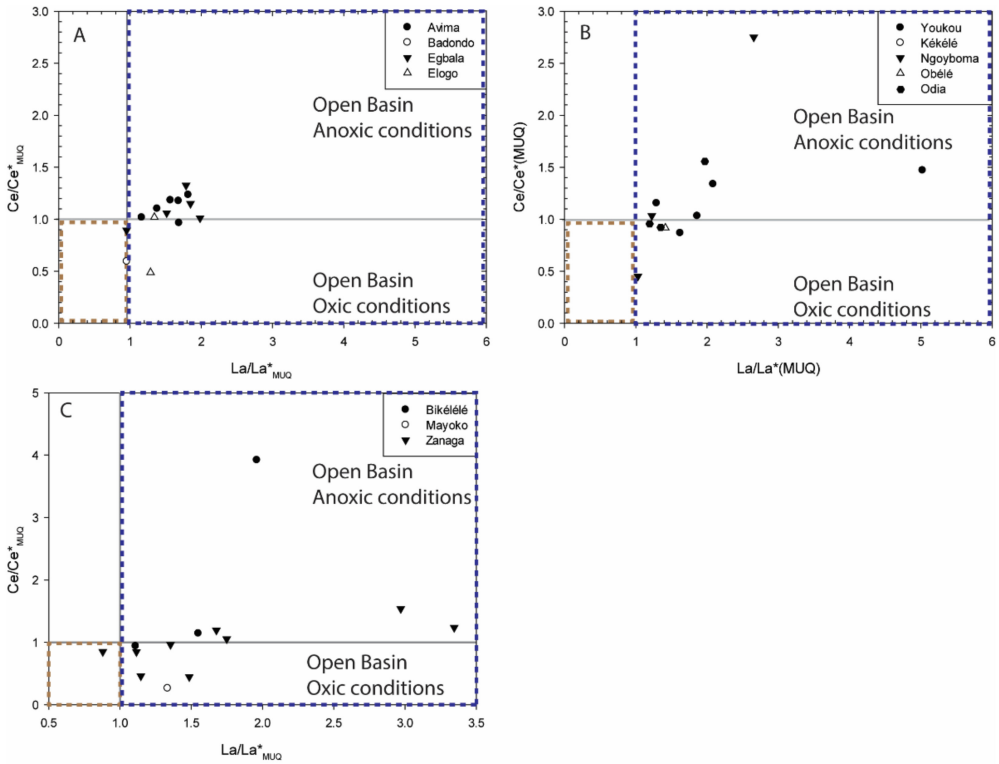


**Figure 9.** Binary plots of Ce/Ce*MUQ versus La/La*MUQ for the Ivindo (**A**), Kelle-Mbomo (**B**) and Chaillu (**C**) blocks. The blue dashed box is the open basin environment, whereas the brown dashed box represents the closed basin in which Fe-oxyhydroxide drives REE-Y scavenging.

Hence, samples ZA6119 and ZNDD182-2 (Zanaga, CAB), which show low Y/Ho ratios (Y/Ho = 21.66 and 27.72) and negative Ce and Y anomalies (Ce/Ce*MUQ = 0.84,

Y/Y*MUQ = 0.62 and 0.95), respectively, and a relatively non-positive to negative La anomaly (La/La*MUQ = 1.11 and 0.87), may suggest precipitation in a closed basin with pH $\geq$ 5, where Fe-oxyhydroxide is the dominant component driving the REE-Y budget (Figure 9c).

Moreover, several negative Ce anomalies are reported from the IAB and CAB (Mayoko and Zanaga BIF samples). They are neither related to negative La and Y excursions nor to low Y/Ho values, suggesting oxic, open-basin depositional conditions (e.g., MO1160-2 from the Mayoko BIF unit, or ZA6210-1 and ZA6210-3 from the Zanaga unit; Figure 8), as recently observed in several Precambrian metasedimentary units [52–54].

These observations indicate a relatively active basin in the IAB and CAB realm, with:

- closed to open basins that may have been affected by sea-level variations;
- pH variations;
- anoxic to oxic water conditions.

The KMAB, however, may reflect only variations of anoxic to locally oxic basin conditions (Figure 9b).

Meanwhile, redox conditions may have constrained the relative depth of sample deposition, suggesting that samples indicating oxic conditions would have been deposited in the photic zone, whereas others would be from deeper, anoxic areas [54].

#### 5.1.3. Sources of the Detrital Components

Detrital components constitute a relatively important feature in basins as they may be used as a proxy for assessing proximal to distal depositional settings in terms of the basin margins, the latter normally being more influenced by such components than the center of a basin far from the coast.

In the IAB, the main detrital sources in these BIFs are felsic rock types (Figure 10). Based on regional geological data, the bright yellow mica schist might represent a possible source for this felsic signature, as already suggested in the literature [25].

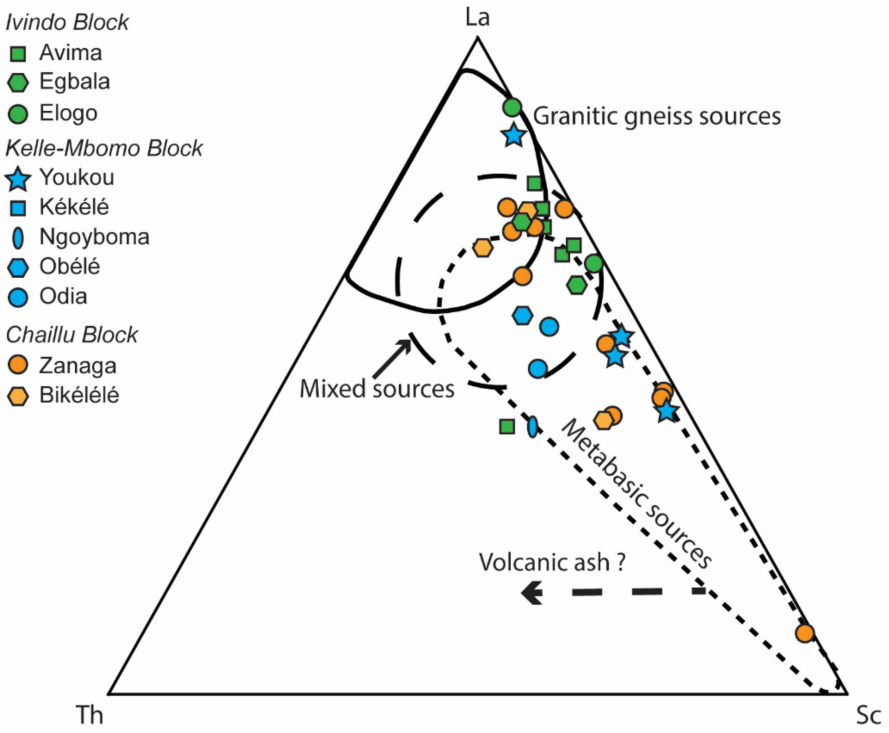


**Figure 10.** Trace element (La-Th-Sc; modified from [55]) plot used for assessing the provenance of detrital components in BIF samples from the Ivindo, Kelle-Mbomo and Chaillu blocks.

Within the KMAB, most samples show a basic affinity (Figure 10), which is again supported by geological mapping at the block scale where mafic rocks are prominent.

In the CAB, the Zanaga BIF unit shows high concentrations and very strong positive correlations ($r > 0.8$) between $Al_2O_3$, $Na_2O$, $TiO_2$ and $K_2O$, $Cr_2O_3$, Sc, V, Cr, Co, Ni, Ga, Sr, and Zr (Figure 7; Table A1). Strong correlation in $Al_2O_3$, $Na_2O$, $TiO_2$, and $K_2O$ is mainly related to weathering of silicate minerals, reflecting river input during sedimentation [42].

The Zr/Hf ratio of 38 confirms the influence of river sediment in this BIF unit as it is relatively close to the chondritic value [56]. These observations suggest the relatively important input from variable detrital sources for this BIF. Figure 10 shows the existence of at least three distinct types of detrital contamination (felsic-intermediate, intermediate-basic, and basic sources) in this BIF unit. Moreover, the ZNDD182-2, ZA6119, and ZNDD209-6 samples, which show variable REE-Y spectra, may indicate a stronger detrital input relative to the other samples, as REE-Y spectra can show negative La and Y and flatter patterns under a detrital influence [7,46,47]. Thus, sample ZNNDD182-2, with a metabasic affinity, is described petrographically by alternating chert layers and greenish material, such as unsubdivided amphibolite, and chlorite is consistent with a detrital source.

Regarding major- and trace element concentrations, high Sc, Mn, Ti, Cr, Co, Ni, and V contents may indicate the leaching of underlying Archean komatiite, tholeiite, and basalt by the vent fluids during Fe-oxyhydroxide precipitation [57,58].

In addition to the fact that Zn may be sourced from mafic volcanic units, it has been suggested that relatively high Zn [59] contents in Archean submarine sedimentary units may be the result of biological activity. Thus, despite ferric-oxyhydroxide particle adsorption, Zn may have occurred in a bio-available form. Biological activity may have occurred at some point in the Zanaga (ZNDD182-2), Obélé (EW5055), and Egbala (SE4471-1 and ME4516) basins based on their relatively high Zn concentrations.

## 6. Conclusions

We present the first relatively exhaustive geochemical datasets for BIFs from the Congo Craton. We sampled and analyzed the Ivindo, Kelle-Mbomo, and Chaillu Archean blocks and BIF units. Their study provided insights into their typical stratigraphic and depositional setting in greenstone belts and provided information concerning the Craton's paleo-geomorphology (distribution of Archean basins and relative distances from basin borders and hydrothermal sources).

Despite the strong tropical weathering observed in Congo, most of the sampled BIF units show LREE depletion relative to HREE and positive La, Y, and Eu anomalies, suggesting deposition in a marine basin under the influence of high-temperature (>250 °C) hydrothermal fluids. This is the typical of the environment of Algoma-type BIFs.

We assessed redox and pH conditions of these paleo-basins based on Ce anomalies and REE + Y patterns. This suggested oxic, open-basin conditions for the Ivindo and Chaillu blocks (Mayoko and Zanaga BIF samples). This observation is important as it suggests that free oxygen was present in early Archean basins.

Algoma-type BIFs act as a favorable host rock for iron mineralization (intrinsic geochemical composition) and orogenic gold within several Archean cratons. Moreover, they may be used as a proxy for hydrothermal-related occurrences regarding their corresponding distance to the hydrothermal vent sources.

**Supplementary Materials:** The following supporting information can be downloaded at https://www.mdpi.com/article/10.3390/min12020114/s1, Table S1: Chemical composition of the sampled BIF samples-major element (wt.%) trace elements (ppm).

**Author Contributions:** Conceptualization, B.G. and O.B.; methodology, B.G.; formal analysis, Y.C., B.G. and O.B.; investigation, B.G.; writing—original draft preparation, B.G. and O.B.; writing—review and editing, B.G., O.B., Y.C., M.C., F.B. and L.-M.J.D.; project administration, Y.C.; funding acquisition, Y.C., F.B. and L.-M.J.D. All authors have read and agreed to the published version of the manuscript.

**Funding:** This study was carried out in the framework of the geological mapping program of the Republic of Congo and was financed by Energy and Mining ASP Inc. referring to the funding numbers: BRGM/DAF/JAC/JUR/PEZ/n°2013/219fr and BRGM/DAF/JAC/JUR/PEZ/n°2013/219co. Thus, the authors thank Asperbras and the Ministry of Mines and Geology of the Republic of the Congo for their support.

**Acknowledgments:** This manuscript forms part of mapping campaigns supported by the mining Asperbras Group (2013–2016). The authors deeply thank the Asperbras Company and the Ministry of Mines and Geology from the Republic of the Congo for their support. The authors gratefully acknowledge all the samplers involved in the BRGM campaign including, Eric Gloaguen, Benjamin Le Bayon, Christian Johannes, Thomas Fullgraf and Florent Boudzoumou. We also thank Phil Thurston from the Harquail School of Mines at Laurentian University (Sudbury, Canada) for his English review and advice on the manuscript. H.M. Kluijver reviewed the final version of the manuscript. We further acknowledge the contributions of two anonymous reviewers, whose constructive comments significantly improved the manuscript.

**Conflicts of Interest:** The authors declare no conflict of interest.

## Appendix A

Appendix A: Linear inter-element correlations for the Zanaga BIF unit. Bold characters highlight significant correlations between elements.

**Table A1.** Linear inter-element correlations for the Zanaga BIF unit. Bold characters highlight significant correlations between elements.

| | $SiO_2$ | $Fe_2O_3$ | CaO | MgO | $Al_2O_3$ | MnO | $Na_2O$ | $Cr_2O_3$ | SrO | BaO | $TiO_2$ | $K_2O$ | $P_2O_5$ | Sc | V | Cr | Co | Ni | Cu | Zn | Ga | Se | Rb | Sr | Zr | Mo | Cd | Sb | Te | Ba | Ta | W | Tl | Pb | Bi | Th | U |
|---|---|---|---|---|---|---|---|---|---|---|---|---|---|---|---|---|---|---|---|---|---|---|---|---|---|---|---|---|---|---|---|---|---|---|---|---|
| **$SiO_2$** | 1.00 | | | | | | | | | | | | | | | | | | | | | | | | | | | | | | | | | | | |
| **$Fe_2O_3$** | 0.28 | 1.00 | | | | | | | | | | | | | | | | | | | | | | | | | | | | | | | | | | |
| **CaO** | −0.60 | **−0.94** | 1.00 | | | | | | | | | | | | | | | | | | | | | | | | | | | | | | | | | |
| **MgO** | −0.53 | **−0.93** | **0.96** | 1.00 | | | | | | | | | | | | | | | | | | | | | | | | | | | | | | | | |
| **$Al_2O_3$** | −0.69 | **−0.88** | **0.98** | **0.92** | 1.00 | | | | | | | | | | | | | | | | | | | | | | | | | | | | | | | |
| **MnO** | −0.37 | −0.80 | 0.79 | 0.84 | 0.72 | 1.00 | | | | | | | | | | | | | | | | | | | | | | | | | | | | | | |
| **$Na_2O$** | −0.70 | −0.80 | **0.91** | **0.94** | **0.91** | 0.84 | 1.00 | | | | | | | | | | | | | | | | | | | | | | | | | | | | | |
| **$Cr_2O_3$** | −0.70 | **−0.88** | **0.99** | **0.94** | **0.99** | 0.72 | 0.92 | 1.00 | | | | | | | | | | | | | | | | | | | | | | | | | | | | |
| **SrO** | −0.64 | −0.86 | **0.96** | 0.85 | **0.97** | 0.71 | 0.83 | 0.96 | 1.00 | | | | | | | | | | | | | | | | | | | | | | | | | | | |
| **BaO** | −0.18 | −0.08 | 0.10 | 0.27 | 0.08 | 0.56 | 0.46 | 0.08 | −0.02 | 1.00 | | | | | | | | | | | | | | | | | | | | | | | | | | |
| **$TiO_2$** | −0.71 | **−0.87** | **0.98** | **0.93** | 1.00 | 0.71 | 0.92 | **1.00** | 0.96 | 0.08 | 1.00 | | | | | | | | | | | | | | | | | | | | | | | | | |
| **$K_2O$** | −0.09 | −0.19 | 0.16 | 0.33 | 0.12 | 0.66 | 0.47 | 0.11 | 0.04 | **0.98** | 0.11 | 1.00 | | | | | | | | | | | | | | | | | | | | | | | | |
| **$P_2O_5$** | 0.38 | −0.40 | 0.18 | 0.40 | 0.04 | 0.48 | 0.23 | 0.06 | −0.05 | 0.46 | 0.05 | 0.54 | 1.00 | | | | | | | | | | | | | | | | | | | | | | | |
| **Sc** | −0.77 | −0.80 | **0.96** | **0.88** | **0.98** | 0.66 | **0.89** | **0.99** | **0.96** | 0.03 | **0.99** | 0.05 | −0.05 | 1.00 | | | | | | | | | | | | | | | | | | | | | | |
| **V** | −0.71 | **−0.87** | **0.98** | **0.94** | **0.99** | 0.71 | 0.92 | **1.00** | **0.96** | 0.09 | **1.00** | 0.11 | 0.06 | **0.99** | 1.00 | | | | | | | | | | | | | | | | | | | | | |
| **Cr** | −0.70 | **−0.87** | **0.98** | **0.93** | **0.99** | 0.72 | 0.92 | **1.00** | **0.96** | 0.07 | **1.00** | 0.10 | 0.04 | **0.99** | **1.00** | 1.00 | | | | | | | | | | | | | | | | | | | | |
| **Co** | −0.72 | −0.86 | **0.98** | **0.93** | **1.00** | 0.72 | 0.92 | **1.00** | **0.96** | 0.10 | **1.00** | 0.12 | 0.04 | **0.99** | **1.00** | **1.00** | 1.00 | | | | | | | | | | | | | | | | | | | |
| **Ni** | −0.70 | **−0.88** | **0.99** | **0.94** | **1.00** | 0.72 | 0.92 | **1.00** | **0.96** | 0.08 | **1.00** | 0.11 | 0.06 | **0.99** | **1.00** | **1.00** | **1.00** | 1.00 | | | | | | | | | | | | | | | | | | |
| **Cu** | 0.04 | −0.26 | 0.20 | 0.08 | 0.26 | 0.15 | 0.06 | 0.16 | 0.28 | −0.10 | 0.18 | 0.01 | −0.23 | 0.12 | 0.15 | 0.16 | 0.19 | 0.18 | 1.00 | | | | | | | | | | | | | | | | | |
| **Zn** | −0.41 | **−0.92** | **0.93** | **0.87** | **0.88** | **0.88** | 0.79 | **0.87** | **0.92** | 0.12 | **0.86** | 0.25 | 0.25 | **0.82** | 0.85 | 0.87 | 0.86 | 0.86 | 0.33 | 1.00 | | | | | | | | | | | | | | | | |
| **Ga** | −0.77 | −0.81 | **0.95** | **0.87** | **0.98** | 0.70 | 0.88 | **0.97** | **0.97** | 0.08 | **0.98** | 0.11 | −0.04 | **0.98** | 0.97 | 0.97 | **0.98** | 0.97 | 0.25 | 0.86 | 1.00 | | | | | | | | | | | | | | | |
| **Se** | 0.35 | −0.28 | 0.10 | 0.05 | 0.10 | 0.20 | −0.04 | 0.01 | 0.13 | 0.03 | 0.03 | 0.17 | 0.14 | −0.06 | 0.00 | 0.00 | 0.03 | 0.03 | **0.87** | 0.30 | 0.09 | 1.00 | | | | | | | | | | | | | | |
| **Rb** | 0.01 | 0.01 | −0.04 | 0.14 | −0.07 | 0.49 | 0.30 | −0.08 | −0.16 | **0.98** | −0.08 | **0.98** | 0.51 | −0.14 | −0.08 | −0.09 | −0.07 | −0.08 | −0.04 | 0.05 | −0.08 | 0.14 | 1.00 | | | | | | | | | | | | | |
| **Sr** | −0.53 | **−0.95** | **0.98** | 0.98 | **0.95** | **0.87** | 0.93 | **0.95** | **0.91** | 0.24 | **0.95** | 0.31 | 0.32 | **0.91** | **0.95** | **0.95** | **0.95** | 0.95 | 0.18 | **0.94** | **0.91** | 0.13 | 0.11 | 1.00 | | | | | | | | | | | | |
| **Zr** | −0.72 | −0.83 | 0.96 | **0.87** | **0.99** | 0.67 | 0.87 | **0.98** | **0.97** | 0.02 | **0.98** | 0.05 | −0.08 | **0.97** | **0.98** | **0.98** | **0.98** | **0.98** | 0.34 | 0.86 | **0.98** | 0.13 | −0.13 | **0.91** | 1.00 | | | | | | | | | | | |
| **Mo** | 0.03 | −0.57 | 0.47 | 0.42 | 0.47 | 0.37 | 0.25 | 0.40 | 0.45 | −0.22 | 0.42 | −0.08 | 0.16 | 0.34 | 0.39 | 0.39 | 0.41 | 0.41 | 0.66 | 0.55 | 0.41 | 0.58 | −0.20 | 0.46 | 0.47 | 1.00 | | | | | | | | | | |
| **Cd** | −0.34 | 0.41 | −0.22 | −0.17 | −0.20 | 0.11 | 0.13 | −0.16 | −0.21 | 0.67 | −0.17 | 0.56 | −0.15 | −0.11 | −0.16 | −0.15 | −0.15 | −0.18 | −0.42 | −0.23 | −0.12 | −0.47 | 0.62 | −0.17 | −0.21 | −0.72 | 1.00 | | | | | | | | | |
| **Sb** | 0.35 | 0.19 | −0.28 | −0.18 | −0.35 | −0.48 | −0.35 | −0.27 | −0.41 | −0.40 | −0.29 | −0.46 | 0.22 | −0.30 | −0.27 | −0.27 | −0.30 | −0.28 | −0.61 | −0.44 | −0.44 | −0.55 | −0.40 | −0.30 | −0.38 | −0.29 | −0.24 | 1.00 | | | | | | | | |
| **Te** | 0.23 | −0.53 | 0.37 | 0.35 | 0.27 | 0.65 | 0.20 | 0.22 | 0.36 | 0.12 | 0.22 | 0.33 | 0.46 | 0.15 | 0.20 | 0.22 | 0.22 | 0.22 | 0.44 | 0.67 | 0.27 | 0.60 | 0.21 | 0.44 | 0.25 | 0.63 | −0.32 | −0.44 | 1.00 | | | | | | | |
| **Ba** | −0.03 | −0.16 | 0.11 | 0.30 | 0.06 | 0.60 | 0.42 | 0.06 | −0.03 | **0.97** | 0.06 | 0.99 | 0.61 | −0.01 | 0.07 | 0.05 | 0.07 | 0.06 | −0.05 | 0.18 | 0.05 | 0.15 | **0.98** | 0.27 | −0.01 | −0.16 | 0.54 | −0.36 | 0.26 | 1.00 | | | | | | |
| **Ta** | −0.79 | −0.60 | 0.79 | 0.73 | 0.82 | 0.48 | 0.71 | 0.83 | 0.79 | −0.04 | 0.83 | −0.05 | −0.02 | **0.87** | 0.83 | 0.82 | 0.83 | 0.83 | −0.07 | 0.65 | **0.87** | −0.17 | −0.20 | 0.74 | 0.80 | 0.13 | −0.08 | −0.16 | 0.06 | −0.06 | 1.00 | | | | | |
| **W** | 0.51 | −0.19 | 0.00 | −0.04 | −0.12 | −0.06 | −0.22 | −0.09 | −0.03 | −0.40 | −0.10 | −0.30 | 0.15 | −0.15 | −0.10 | −0.06 | −0.11 | −0.09 | 0.00 | 0.11 | −0.20 | 0.08 | −0.32 | −0.01 | −0.10 | −0.06 | −0.33 | 0.48 | 0.20 | −0.25 | −0.21 | 1.00 | | | | |

**Table A1.** *Cont.*

| | $SiO_2$ | $Fe_2O_3$ | CaO | MgO | $Al_2O_3$ | MnO | $Na_2O$ | $Cr_2O_3$ | SrO | BaO | $TiO_2$ | $K_2O$ | $P_2O_5$ | Sc | V | Cr | Co | Ni | Cu | Zn | Ga | Se | Rb | Sr | Zr | Mo | Cd | Sb | Te | Ba | Ta | W | Tl | Pb | Bi | Th | U |
|---|---|---|---|---|---|---|---|---|---|---|---|---|---|---|---|---|---|---|---|---|---|---|---|---|---|---|---|---|---|---|---|---|---|---|---|---|
| **Tl** | 0.52 | −0.25 | 0.04 | −0.03 | −0.06 | 0.32 | −0.18 | −0.10 | 0.10 | −0.11 | −0.11 | 0.10 | 0.29 | −0.16 | −0.13 | −0.10 | −0.12 | −0.11 | 0.41 | 0.39 | −0.06 | 0.61 | 0.04 | 0.09 | −0.06 | 0.40 | −0.32 | −0.30 | **0.88** | 0.06 | −0.21 | 0.47 | 1.00 | | | | |
| **Pb** | 0.39 | 0.03 | −0.18 | −0.25 | −0.12 | −0.27 | −0.33 | −0.21 | −0.12 | −0.25 | −0.19 | −0.18 | −0.13 | −0.25 | −0.22 | −0.22 | −0.19 | −0.19 | 0.82 | −0.09 | −0.13 | **0.87** | −0.14 | −0.20 | −0.07 | 0.46 | −0.56 | −0.32 | 0.20 | −0.17 | −0.30 | 0.01 | 0.32 | 1.00 | | | |
| **Bi** | −0.28 | 0.56 | −0.34 | −0.49 | −0.28 | −0.43 | −0.32 | −0.25 | −0.16 | −0.30 | −0.26 | −0.39 | −0.74 | −0.13 | −0.25 | −0.23 | −0.25 | −0.27 | −0.34 | −0.35 | −0.18 | −0.57 | −0.33 | −0.44 | −0.21 | −0.60 | 0.50 | 0.06 | −0.44 | −0.42 | 0.00 | 0.04 | −0.21 | −0.41 | 1.00 | | |
| **Th** | 0.00 | −0.23 | 0.20 | 0.06 | 0.23 | 0.33 | 0.09 | 0.14 | 0.32 | 0.03 | 0.16 | 0.17 | −0.23 | 0.12 | 0.13 | 0.14 | 0.17 | 0.15 | **0.89** | 0.43 | 0.27 | 0.78 | 0.11 | 0.19 | 0.30 | 0.62 | −0.19 | −0.81 | 0.64 | 0.06 | −0.09 | −0.08 | 0.60 | 0.59 | −0.17 | 1.00 | |
| **U** | −0.40 | 0.39 | −0.16 | −0.27 | −0.10 | −0.24 | −0.20 | −0.12 | −0.05 | −0.17 | −0.11 | −0.22 | −0.38 | 0.01 | −0.11 | −0.13 | −0.10 | −0.12 | −0.16 | −0.16 | 0.07 | −0.20 | −0.19 | −0.22 | −0.06 | −0.30 | 0.23 | −0.20 | −0.13 | −0.23 | 0.41 | −0.39 | −0.10 | −0.10 | 0.54 | −0.05 | 1.00 |

## References


1. James, H.L. Sedimentary facies of iron-formation. *Econ. Geol.* **1954**, *49*, 235–293. [CrossRef]
2. Goodwin, A.M. Archean iron-formations and tectonic basins of the Canadian Shield. *Econ. Geol.* **1973**, *68*, 915–933. [CrossRef]
3. Bekker, A.; Slack, J.F.; Planavsky, N.; Krapez, B.; Hofmann, A.; Konhauser, K.O.; Rouxel, O.J. Iron formation: The sedimentary product of a complex interplay among mantle, tectonic, oceanic, and biospheric processes. *Econ. Geol.* **2010**, *105*, 467–508. [CrossRef]
4. Huston, D.L.; Logan, G.A. Barite, BIFs and bugs: Evidence for the evolution of the Earth's early hydrosphere. *Earth Planet. Sci. Lett.* **2004**, *220*, 41–55. [CrossRef]
5. Van den Boorn, S.H.J.M.; Van Bergen, M.J.; Vroon, P.Z.; de Vries, S.T.; Nijman, W. Silicon isotope and trace element constraints on the origin of 3.5 Ga cherts: Implications for early Archaean marine environments. *Geochim. Cosmochim. Acta* **2010**, *74*, 1077–1103. [CrossRef]
6. Hickman-Lewis, K.; Gourcerol, B.; Westall, F.; Manzini, D.; Cavalazzi, B. Reconstructing Palaeoarchaean microbial biomes flourishing in the presence of emergent landmasses using trace and rare earth element systematics. *Precambrain Res.* **2020**, *342*, 105689. [CrossRef]
7. Gourcerol, B.; Thurston, P.; Kontak, D.; Côté-Mantha, O.; Biczok, J. Depositional setting of Algoma-type banded iron formation. *Precambrain Res.* **2016**, *281*, 47–79. [CrossRef]
8. Gourcerol, B.; Kontak, D.J.; Thurston, P.C.; Duparc, Q. Do Magnetite layers in Algoma-Type Banded Iron Formations (BIF) preserve their primary geochemical signature? A case study of samples from three Archean BIF-hosted gold deposits. *Can. Mineral.* **2016**, *54*, 605–624. [CrossRef]
9. Araújo, J.C.S.; Lobato, L.M. Depositional model for banded iron formation host to gold in the Archean Rio das Velhas greenstone belt, Brazil, based on geochemistry and LA-ICP-MS magnetite analyses. *J. S. Am. Earth Sci.* **2019**, *94*, 102205. [CrossRef]
10. Ilouga, C.D.I.; Suh, C.E.; Ghogomu, R.T. Textures and rare earth elements composition of Banded Iron Formations (BIF) at Njweng prospect, Mbalam Iron Ore District, Southern Cameroon. *Int. J. Earth Sci.* **2013**, *4*, 146–165. [CrossRef]
11. Ilouga, D.C.I.; Ndong Bidzang, F.; Ziem A. Bidias, L.A.; Olinga, J.B.; Tata, E.; Minyem, D. Geochemical characterization of a stratigraphic log bearing iron ore in the Sanaga prospect, Upper Nyong Unit of Ntem Complex, Cameroon. *Int. J. Geosci. Geomat.* **2017**, *5*, 218–228.
12. Ganno, S.; Ngnotue, T.; Kouankap Nono, G.D.; Nzenti, J.P.; Notsa Fonkeng, M. Petrology and geochemistry of the banded iron-formations from Ntemcomplex greenstones belt, Elom area, Southern Camroon: Implications for the origin and depositional environment. *Geochemistry* **2015**, *75*, 375–387.
13. Ganno, S.; Njiosseu Tanko, E.L.; Kouankap, N.G.D.; Djoukouo Soh, A.; Moudioh, C.; Ngnotue, T.; Nzenti, J.P. A mixed seawater and hydrothermal origin of superior-type banded iron formation (BIF)-hosted Kouambo iron deposit, Palaeoproterozoic Nyong series, Southwestern Cameroon: Constraints from petrography and geochemistry. *Ore Geol. Rev.* **2017**, *80*, 860–875.
14. Teutsong, T.; Bontognali, T.R.R.; Ndjiogui, P.-D.; Vrijmoed, J.C.; Teagle, D.; Cooper, M.; Vance, D. Petrography and geochemistry of the Mesoarchean Bikoula banded iron formation in the Ntem complex (Congo Craton), Southern Cameroon. Implications for its origin. *Ore Geol. Rev.* **2017**, *80*, 267–288. [CrossRef]
15. Ndime, E.N.; Ganno, S.; Soh Tamehe, L.; Nzenti, J.P. Petrography, lithostratigraphy and major element geochemistry of Mesoarchean metamorphosed banded iron formation-hosted Nkout iron ore deposit, north western Congo craton, Central West Africa. *J. Afr. Earth Sci.* **2019**, *148*, 80–98. [CrossRef]
16. Moudioh, C.; Soh Tamehe, L.; Ganno, S.; Nzepang Tankwa, M.; Brando Soares, M.; Ghosh, R.; Kankeu, J.; Nzentia, P. Tectonic setting of the Bipindi greenstone belt, northwest Congo craton, Cameroon: Implications on BIF deposition. *J. Afr. Earth Sci.* **2020**, *171*, 103971. [CrossRef]
17. Soh Tamehe, L.; Nzepang, T.M.; Wei, C.T.; Ganno, S.; Ngnotue, T.; Kouankap, N.G.D.; Simon, S.J.; Zhang, J.J.; Nzenti, J.P. Geology and geochemical constrains on the origin and depositional setting of the Kpwa–Atog Boga banded iron formations (BIFs), northwestern Congo craton, southern Cameroon. *Ore Geol. Rev.* **2018**, *95*, 620–638. [CrossRef]
18. Soh Tamehe, L.; Chongtao, W.; Ganno, S.; Simon, S.J.; Kouankap Nono, G.D.; Nzenti, J.P.; Lembjou, B.Y.; Lin, N.H. Geology of the Gouap iron deposit, Congo craton, southern Cameroon: Implication for iron ore exploration. *Ore Geol. Rev.* **2019**, *107*, 1097–1128. [CrossRef]
19. Retonda Kondja, S.; Ndong Ondo, S.M.; Edou Minko, A.; Mayaga Mikolo, F. The Bélinga Iron Ore Deposit (∼2.8 Ga), NE-Gabon: Reactualization and new interpretations on crests. *Eur. Sci. J.* **2017**, *13*, 307–321.
20. Thiéblemont, D.; Liégeois, J.P.; Fernandez-Alonso, M.; Ouabadi, A.; Le Gall, B.; Maury, R.; Jalludin, M.; Vidal, M.; Ouattara-Gbélé, C.; Tchaméni, R.; et al. *Geological Map of Africa at 1:10 M Scale*; Editors CGMW-BRGM: Orléans, France, 2016.
21. Thiéblemont, D.; Castaing, C.; Billa, M.; Bouton, P.; Préat, A. *Notice Explicative de la Carte Géologique et des Ressources Minérales de la République Gabonaise à 1/1 000 000*; Editor DGMG—Ministère des Mines, du Pétrole, des Hydrocarbures: Libreville, Gabon, 2009; p. 381.
22. Chevallier, L.; Makanga, J.F.; Thomas, R.J. *Notice Explicative de la Carte Géologique de la République Gabonaise à 1/1 000 000*; Editions DGMG Gabon: Libreville, Gabon, 2002; p. 195.
23. Blein, O.; Callec, Y.; Fullgraf, T.; Chevillard, M.; Cagnard, F.; Bauer, H.; Prognon, F.; Badinier, G.; Vic, G.; Boudzoumou, F.; et al. *Notice Explicative de la Carte Géologique de la République Du Congo à 1/200 000, Feuille Mbomo*; Editor BRGM: Brazzaville, République du Congo, 2017; 206p.

24. Chevillard, M.; Fullgraf, T.; Blein, O.; Badinier, G.; Boudzoumou, F.; Joannes, C.; Rouzeau, O.; Callec, Y. *Carte Géologique de la République du Congo à 1/200 000, Feuille Ewo*; Editor BRGM: Brazzaville, République du Congo, 2017; 1p.
25. Fullgraf, T.; Blein, O.; Le Bayon, B.; Cagnard, F.; Boudzoumou, F.; Joannes, C.; Chevillard, M.; Melleton, J.; Callec, Y. *Notice Explicative de la Carte Géologique de la République du Congo à 1/200 000, Feuille Mékambo-Mintom*; Editor BRGM: Brazzaville, République du Congo, 2017; 148p.
26. Gloaguen, E.; Chevillard, M.; Fullgraf, T.; Blein, O.; Boudzoumou, F.; Joannes, C.; Badinier, G.; Issautier, B.; Callec, Y.; Madous, P.L.; et al. *Carte Géologique de la République du Congo à 1/200 000, Feuille Zanaga*; Editor BRGM: Brazzaville, République du Congo, 2017; 1p.
27. Issautier, B.; Chevillard, M.; Fullgraf, T.; Callec, Y.; Le Bayon, B.; Schroetter, J.-M.; Gloaguen, E.; Blein, O.; Prognon, F.; Badinier, G.; et al. *Carte Géologique de la République du Congo à 1/200 000, Feuille Sembé-Souanké*; Editor BRGM: Brazzaville, République du Congo, 2017; 1p.
28. Chevillard, M.; Fullgraf, T.; Blein, O.; Bauer, H.; Prognon, F.; Badinier, G.; Vic, G.; Boudzoumou, F.; Loumbi Tatinéné, C.M.; Ngandziami, P.V.; et al. *Carte Géologique de la République Du Congo à 1/200 000, Feuille Mbomo*; Editor BRGM: Brazzaville, République du Congo, 2017; 1p.
29. Chevillard, M.; Callec, Y.; Gloaguen, E.; Paquet, F.; Serrano, O.; Fullgraf, T.; Blein, O.; Boudzoumou, F.; Joannes, C.; Devoir, A.; et al. *Carte Géologique de la République Du Congo à 1/200 000, Feuille Mossendjo*; Editor BRGM: Brazzaville, République du Congo, 2017; 1p.
30. Chevillard, M.; Gloaguen, E.; Fullgraf, T.; Blein, O.; Callec, Y.; Paquet, F.; Serrano, O.; Melleton, J.; Boudzoumou, F.; Cagnard, F.; et al. *Notice Explicative de la Carte Géologique de la République Du Congo à 1/200 000, Feuille Mossendjo*; Editor BRGM: Brazzaville, République du Congo, 2017; 159p.
31. Thiéblemont, D.; Agenbacht, A.; Boulingui, B.; Bouton, P.; Ekogha, H.; Goujou, J.C.; Kassadou, A.B.; Moussavou, M.; Prian, J.P.; Theunissen, K.; et al. Synchronous BIF, HT metamorphism and granitic plutonism at ca. 2.8 Ga in Gabon. In Proceedings of the 23th Congress on African Geology, Johannesburg, South Africa, 11–14 January 2011.
32. Cunningham, M.; De Waele, B. Geological mapping of Badondo and iron mineralization targets, Republic of the Congo. *Struct. Geol. Resour.* **2012**, *54*, 54–56.
33. Avima Iron Ore. 2016. Available online: http://avimairon.com/avima.html (accessed on 16 January 2022).
34. Gates Ebotehouna, C.; Xie, Y.; Adomako-Ansah, K.; Gourcerol, B.; Qu, Y. Depositional setting and genesis of the Nabeba BIF hosting high-grade iron ore deposit, NW of the Republic Congo. *Minerals* **2021**, *11*, 579.
35. Caen-Vachette, M.; Vialette, Y.; Bassot, J.P.; Vidal, P. Apport de la géochronologie isotopique à la connaissance de la géologie gabonaise. *Chron. Rech. Min.* **1988**, *491*, 35–53.
36. Bouton, P.; Thiéblemont, D.; Gouin, J.; Cocherie, A.; Guerrot, C.; Tegyey, M.; Préat, A.; Simo Ndounze, S.; Moussavou, M. *Notice Explicative de la Carte Géologique de la République du Gabon à 1/200 000, Feuille Franceville-Boumango*; Edition DGMG-Ministère des Mines, du Pétrole, des Hydrocarbures: Libreville, Gabon, 2009; p. 79.
37. Sindhuja, C.S.; Manikyamba, C.; Pahari, A.; Satyanarayanan, M. Geochemistry of banded sulphidic cherts of Sandur greenstone belt, Dharwar Craton, India: Constraints on hydrothermal processes and gold mineralization. *Ore Geol. Rev.* **2020**, *122*, 103529. [CrossRef]
38. Lawrence, M.G.; Kamber, B.S. The behavior of the rare earth elements during estuarine mixing—Revisited. *Mar. Chem.* **2006**, *100*, 147–161. [CrossRef]
39. Bonnand, P.; Lalonde, S.V.; Boyeta, M.; Heubeck, C.; Homann, M.; Nonnotte, P.; Foster, I.; Konhauser, K.O.; Köhler, I. Post-depositional REE mobility in a Paleoarchean banded iron formation revealed by La-Ce geochronology: A cautionary tale for signals of ancient oxygenation. *Earth Planet. Sci. Lett.* **2020**, *547*, 116452. [CrossRef]
40. Mukhopadhyay, J.; Crowley, Q.G.; Ghosh, S.; Ghosh, G.; Chakrabarti, K.; Misra, B.; Heron, K.; Bose, S. Oxygenation of the Archean atmosphere: New paleosol constraints from eastern India. *Geology* **2014**, *42*, 923–926. [CrossRef]
41. Danielson, A.; Möller, P.; Dulski, P. The europium anomalies in banded iron formations and the thermal history of the oceanic crust. *Chem. Geol.* **1992**, *97*, 89–100. [CrossRef]
42. Bau, M.; Dulski, P. Comparing yttrium and rare earths in hydrothermal fluids from the Mid-Atlantic Ridge: Implications for Y and REE behaviour during near- vent mixing and for the Y/Ho ratio of Proterozoic seawater. *Chem. Geol.* **1999**, *155*, 77–90. [CrossRef]
43. Allwood, A.C.; Kamber, B.S.; Walter, M.R.; Burch, I.W.; Kanik, I. Trace element record depositional history of an Early Archean stromatolitic carbonate platform. *Chem. Geol.* **2010**, *270*, 148–163. [CrossRef]
44. Thurston, P.C.; Kamber, B.S.; Whitehouse, M. Archean cherts in banded iron formation: Insight into Neoarchean ocean chemistry and depositional processes. *Precambrian Res.* **2012**, *214*, 227–257. [CrossRef]
45. Nesbitt, H.W. Mobility and fractionation of rare earth elements during weathering of granodiorite. *Nature* **1979**, *279*, 206–210. [CrossRef]
46. Gourcerol, B.; Thurston, P.C.; Kontak, D.J.; Côté-Mantha, O. Interpretations and implications of LA ICP-MS analysis of chert for the origin of geochemical signatures in banded iron formations (BIFs) from the Meadowbank gold deposit, Western Churchill Province, Nunavut. *Chem. Geol.* **2015**, *410*, 89–107. [CrossRef]

47. Alexander, B.W.; Bau, M.; Andersson, P.; Dulski, P. Continentally-derived solutes in shallow Archean sea water; rare earth element and Nd isotope evidence in iron formation from the 2.9 Ga Pongola Supergroup, South Africa. *Geochim. Cosmochim. Acta* **2008**, *72*, 378–394. [CrossRef]
48. Alibo, D.S.; Nozaki, Y. Rare earth elements in seawater: Particle association, shale-normalization, and Ce oxidation. *Geochim. Cosmochim. Acta* **1999**, *63*, 363–372. [CrossRef]
49. Kawabe, I.; Ohta, A.; Ishii, S.; Tokumura, M.; Miyauchi, K. REE partitioning between Fe-Mn oxyhydroxide precipitates and weakly acid NaCl solutions: Convex tetrad effect and fractionation of Y and Sc from heavy lanthanides. *Geochem. J.* **1999**, *33*, 167–179. [CrossRef]
50. Bau, M.; Koschinsky, A. Oxidative scavenging of cerium on hydrous Fe oxide: Evidence from distribution of rare earth elements and yttrium between Fe oxides and Mn oxides in hydrogenetic ferro manganeses crusts. *Geochem. J.* **2008**, *43*, 37–47. [CrossRef]
51. Bau, M. Scavenging of dissolved yttrium and rare earths by precipitating iron oxyhydroxide: Experimental evidence for Ce oxidation, Y-Ho fractionation, and lanthanide tetrad effect. *Geochim. Cosmochim. Acta* **1999**, *63*, 67–77. [CrossRef]
52. Rouxel, O.J.; Bekker, A.; Edwards, K.J. Iron Isotope Constraints on the Archean and Paleoproterozoic Ocean Redox State. *Science* **2005**, *307*, 1088–1091. [CrossRef]
53. Fralick, P.; Riding, R. Steep Rock Lake: Sedimentology and geochemistry of an Archean carbonate platform. *Earth-Sci. Rev.* **2015**, *151*, 132–175. [CrossRef]
54. Swanner, E.D.; Maisch, M.; Wu, W.; Kappler, A. Oxic Fe(III)reduction could have generated Fe(II) in the photic zone of Precambrian seawater. *Nature* **2018**, *8*, 4238. [CrossRef]
55. Bhatia, M.R.; Crook, K.A.W. Trace element characteristics of graywackes and tectonic setting discrimination of sedimentary basins. *Contrib. Mineral. Petrol.* **1986**, *92*, 181–193. [CrossRef]
56. Bau, M.; Alexander, B.W. Distribution of high field strength elements (Y, Zr, REE, Hf, Ta, Th, U) in adjacent magnetite and chert bands and in reference standards FeR-3 and FeR-4 from the Temagami iron-formation, Canada, and the redox level of the Neoarchean ocean. *Precambrain Res.* **2009**, *174*, 337–346. [CrossRef]
57. Pecoits, E.; Gringas, M.K.; Barley, M.E.; Kappler, A.; Posth, N.R.; Konhauser, K.O. Petrography and geochemistry of the Dales Gorge banded iron formation: Paragenetic sequence, source and implications for palaeo-ocean chemistry. *Precambrain Res.* **2009**, *172*, 163–187. [CrossRef]
58. Dare, S.A.S.; Beaudoin, G.; Méric, J.; Boutroy, E.; Potvin-Doucet, C. Trace elements in magnetite as petrogenetic indicators. *Miner. Depos.* **2014**, *49*, 785–796. [CrossRef]
59. Mloszewska, A.M.; Pecoits, E.; Cates, N.L.; Mojzsis, S.J.; O'Neil, J.; Robbins, L.J.; Konhauser, K.O. The compositon of Earth's oldest iron formations: The Nuvvuagittuq Supracrustal belt (Québec, Canada). *Earth Planet. Sci. Lett.* **2012**, *317*, 331–342. [CrossRef]